IEEE Access
Multidisciplinary | Rapid Review | Open Access Journal

Received 5 June 2023, accepted 22 June 2023, date of publication 3 July 2023, date of current version 13 July 2023.

Digital Object Identifier 10.1109/ACCESS.2023.3291814

RESEARCH ARTICLE

A Ka-Band Deployable Active Phased Array Transmitter Fabricated on 4-Layer Liquid Crystal Polymer Substrate for Small-Satellite Mount

DONGWON YOU[1], (Graduate Student Member, IEEE), XIAOLIN WANG[1], (Student Member, IEEE), HANS HERDIAN[1], (Member, IEEE), XI FU[1], (Graduate Student Member, IEEE), HOJUN LEE[1], MICHIHIRO IDE[1], (Graduate Student Member, IEEE), CARREL DA GOMEZ[1], (Graduate Student Member, IEEE), ZHENG LI[1], (Graduate Student Member, IEEE), JILL MAYEDA[1], (Member, IEEE), DAISUKE AWAJI[2], JIAN PANG[1], (Member, IEEE), HIRAKU SAKAMOTO[3], KENICHI OKADA[1], (Fellow, IEEE), AND ATSUSHI SHIRANE[1], (Member, IEEE)

[1]Department of Electrical Engineering, Tokyo Institute of Technology, Meguro City, Tokyo 152-8552, Japan
[2]Wideband Radio System Development, Electronic Technologies Research and Development Center, Fujikura Ltd., Koto City, Tokyo 135-8512, Japan
[3]Department of Mechanical Engineering, Tokyo Institute of Technology, Meguro City, Tokyo 152-8552, Japan

Corresponding author: Atsushi Shirane (shirane@ee.e.titech.ac.jp)

This work was supported in part by the Ministry of Internal Affairs and Communications (MIC)/Strategic Information and Communications Research and Development Promotion Program (SCOPE) under Grant 192203002 and Grant 192103003; in part by the Japan Society for the Promotion of Science (JSPS) under Grant JP20H00236; in part by the MIC under Grant JPJ000254; in part by the Japan Science and Technology Agency (JST)/Adaptable and Seamless Technology Transfer Program through Target-Driven Research and Development (A-STEP) under Grant JPMJTR211D; in part by the National Institute Of Information and Communications Technology (NICT) under Grant 00601; in part by the (STAR); and in part by the VLSI Design and Education Center (VDEC) in Collaboration with Cadence Design Systems, Inc., Mentor Graphics, Inc., and Keysight Technologies Japan, Ltd.

ABSTRACT Lightweight and deployable phased arrays are important in Small-Satellite (Small-Sat) constellation systems to reduce price and increase link distance. This article proposes a Ka-band deployable active phased-array TX on a 4-layer liquid crystal polymer (LCP) board for a lightweight and high stowage rate solution to break through the trade-off between high antenna aperture size and small form factor in phased arrays. This article describes detailed designs of the phased array and its building blocks with the proposed 4-layer LCP substrate structure. Assembled with the beamformer ICs (BFIC), a Ka-band 8 × 4-element deployable active phased-array TX on the 4-layer LCP substrate is fabricated. The proposed deployable phased-array TX can steer the beam from −50° to 50°. The phased-array TX can drive 32-APSK DVB-S2 signal with a −28.7 dB EVM as well, revealing that the deployable phased-array TX performs with high phased-array performance. Furthermore, the TX achieved the lightest and thinnest phased array with 0.96 kg/m^2 areal mass and 0.9 mm thickness. This groundbreaking research sets the stage for the realization of affordable and user-centric satellite communication (SATCOM) in low-earth orbit (LEO).

INDEX TERMS Deployable, liquid crystal polymer (LCP), phased array, transmitter (TX), satellite communication (SATCOM), 5G, small-satellite.

I. INTRODUCTION

The high data rate low-earth orbit (LEO) satellite communication (SATCOM) turned out to be an inevitable communication paradigm as the LEO SATCOM provides low latency, link survivability, and the link to all of the globes [1], [2], [3], [4]. As terrestrial communication networks are showing their limitations, the importance of high data rate LEO SATCOM is becoming more emphasized. Even though cellular communication networks, such as long-term evolution (LTE)

The associate editor coordinating the review of this manuscript and approving it for publication was Nan Wu.

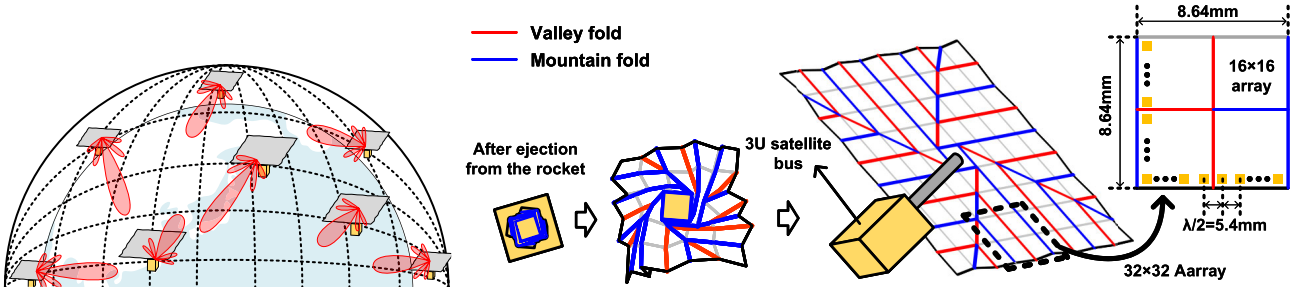

FIGURE 1. Conceptual diagrams of (a) LEO Small-SAT constellation system, and (b) the Ka-band deployable active phased array.

and 5^{th} generation cellular network (5G), cover almost all the area conquered by human beings, the cellular networks with only terrestrial infrastructures have not been able to and will not be able to connect air, maritime, underprivileged areas, and massive terminals from internet of things (IoT) without SATCOM systems. The integration of satellite and terrestrial networks is an essential requirement in the near future [5]. Not only does the communication mission of satellites increase the importance of LEO SATCOM, but the earth-exploration satellite (EES) is also contributing to its significance. The big data generated from optical cameras' imagery data needs to be handled, which highlights the need for LEO SATCOM [4].

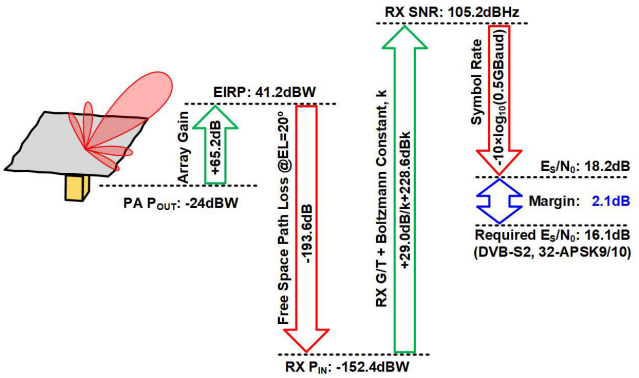

FIGURE 2. A high data rate LEO SATCOM link budget with a 1024-element array under 550km altitude and 20° elevation.

Unlike 5G or LTE terrestrial phased-array systems [6], [7], [8], [9], [10], [11], [12], [13], [14], [15], the key technique in LEO SATCOM is the deployability of the antenna aperture. The requirement of the deployability is derived from low-cost small satellites (Small-SAT) features which makes LEO SATCOM feasible. As the LEO satellites fly at a low altitude of 100 to 1000 km, the communication coverage area is limited. Thus, satellites are enforced to build a satellite constellation with multiple satellites. This, again, results in the need for small-sized satellite designs with a reduced cost of the unit satellite. However, due to the reduced satellite body size, both solar cells for solar energy and antenna aperture size must be reduced.

To cope with a trade-off between antenna aperture size and satellite size, a lot of research on origami techniques such as deployable antenna aperture have been studied [16], [17], [18], [19], [20], [21], [22], [23], [24], [25], [26], [27], [28], [29]. Two separated rigid boards being joined on a textile membrane to implement deployability is reported in [17] with a 4 × 2 array. While this structure is rigid and safe, its areal mass is heavy and it requires additional coaxial cables to connect between two rigid sub-array boards. In [18], [19], and [20], a 16 × 16-element active phased array on polyimide flexible substrate (flex substrate) is reported. Using flex substrate, extremely low weight per area is achieved. However, the loss of polyimide is too large to drive mm-wave signals. Not only are the fully flexible substrates but rigid-flex hybrid substrates are also reported in [21], [22], and [23]. To implement deployability, in [21], element antennas on unit rigid substrates are laminated on polyimide flex substrate. However, laminated rigid and flex substrates inherently have huge process variations. As a result, the laminated rigid-flex hybrid substrate is not suitable for mm-wave phased array antennas. In [22] and [23], an air gap antenna architecture is implemented by floating the ground plane on a rigid substrate and an antenna layer on a flexible substrate. By doing so, low-frequency and low-loss antennas are fabricated even though the loss of the FR-4 substrate is large. This floating ground and antenna layer structure, however, is challenging to build for short wave-length antenna arrays. Antennas on inkjet-printed substrates are also reported in [24] and [25], but this structure also has large process variations. Even worse, antenna air gap thickness errors are not well controlled after deployment.

In this article, a Ka-band deployable CMOS active phased-array transmitter (TX) on a lightweight, high process-accuracy, and low-loss 4-layer liquid crystal polymer (LCP) substrate fabrication is proposed for LEO Small-SATs. The TX is powered by 28 GHz beamformer ICs (BFIC) in [13]. The fabricated phased-array TX in this article is designed as a proof of principle prototype with 8 × 4-element array size. Being supported by the MTT-Sat Challenge, this TX is supposed to be developed to a 32 × 32-element array, launched, and performed in a space demonstration. In order to achieve better performances, prior researches are preceded

and presented in [28] and [29]. While the performance evaluation of single-element antennas is extensively discussed in [29], and the fabrication and evaluation of the initial LCP phased array prototype are documented in [28], this work delves deeper into the design intricacies of each microwave block, providing a comprehensive and detailed layout of the system.

The rest of this paper is organized as follows, the deployable phased array TX system design and LEO Small-SAT constellation system are discussed in Sec. II, including downlink link budget design. Then, various types of deployable array structures will be compared in Sec. III. After that, the proposed phased array, mm-wave components, and their design are described in Sec. IV. Finally, measured data and conclusion follow in Sec. V and Sec. VI, respectively.

II. DEPLOYABLE ARRAY AND LINK BUDGET

A. DEPLOYABLE ARRAY ANTENNA

In order to implement the high data rate LEO Small-SAT constellation system (Fig. 1(a)), a Small-Sat with a 1 m×1 m-size deployable membrane in [30] will be launched as loading the proposed deployable active phased array TX on a 4-layer LCP substrate as presented in Fig. 1(b). The satellite adopts a membrane with a ''flasher'' origami pattern model for centrosymmetricity and high stowage rate [30], [31], [32], [33]. For future space demonstration, a 32 × 32-element deployable active phased array on a 4-layer LCP substrate will be mounted in the membrane. Although this current work only highlights the implementation of the TX with this packaging, these BFICs are composed of transceivers (TRX) to directly communicate with terrestrial TRXs utilizing time division duplex (TDD) mode. All other remaining areas of the membrane including the opposite side of the membrane not only the phased array side will be covered by solar cells. During the daytime, when the satellite is positioned between the sun and the earth, the solar cells located on the plane without the phased array serve as the primary energy generators. Conversely, during the nighttime when the satellite retreats behind the earth, the solar cells on the plane with the phased array become the main energy generators until the satellite is completely enveloped by the shadow cast by the earth. The body of the satellite is formed as a 3U CubeSat, which carries power management units and a microcontroller unit.

B. LINK BUDGET DESIGN

To support the above conceptual idea of the high data rate LEO Small-SAT constellation system, a sophisticated design of a phased-array TX link budget is one of the most important considerations. The link budget of a 1024-element array in a satellite TX with a ground station is shown in Fig. 2. The satellite is supposed to operate from 20° to 160° elevation angle. As the satellite orbits at an altitude of 550 km and at an angle of 20°, the distance from the satellite to the ground station is 1293.8 km, which is 183.6 dB of free space path loss at the 28 GHz center frequency. In the Link budget, 10 dB of additional path losses are assumed from conditions such as rain loss, atmospheric loss, ionospheric loss, and polarization mismatch loss based on International Telecommunication Union (ITU) recommendations [34], [35], [36], [37], [38]. The power amplifier (PA) at each element in the TX array outputs 6 dBm averaged output power. At an orbit altitude of 550 km, a 2.8 m parabola antenna with 29.0 dB/K of G/T in the RX demodulates the signal. To take the worst link distance case into account, an elevation angle of 20° to the RX is assumed in the link budget. The resultant SNR is calculated with the following equation:

$$\frac{S}{N} = P_{TX} \cdot G_{TX} \cdot \left(\frac{\lambda}{4\pi d}\right)^2 \cdot \frac{1}{L_{sum}} \cdot \frac{G_{RX}}{T_{N,RX}} \cdot \frac{1}{k} \cdot \frac{1}{R_S} \quad (1)$$

where P_{TX} is the TX element output power, G_{TX} is the array antenna gain, λ is the center frequency wavelength, d is the distance between the satellite and the ground station, L_{sum} is the sum of all losses except for the free-space path loss, G_{RX} is the receive antenna gain, $T_{N,RX}$ is the noise temperature for the RX, k is the Boltzmann constant, and R_S is the symbol rate. For the modulated signal, DVB-S2, 32-APSK 9/10 signal with 0.5 GBaud symbol rate is used. From the link budget results, if the full size of the array is implemented, 2.5 Gbps of high data rate communication is supported.

III. COMPARISON OF DEPLOYABLE ARRAYS

Selection of the appropriate substrate for deployability is the key to the success of a small form factor satellite with a large antenna aperture area. To build deployable active phased arrays, a lot of layers in a substrate are required. This is because active devices, such as amplifiers and phase shifters, require lots of ports and wires for controls and DC power distributions, which, again, require complex and wide areas of metal patterns. For this reason, a multi-layer substrate is preferred. In addition to the multi-layer feature, the flexibility of the substrate is one more important consideration for deployability. A few studies have been reported to develop deployable phased arrays and they are summarized in Table 1. As it can be rarely found in the pieces of literature, multi-layer flexible substrate fabrication is very challenging. To the best of the author's knowledge, this work and the work in [18] are the only works for deployable active phased arrays on the flexible substrate with the largest number of layers in the literature. Together with the above two important considerations, several other major parameters are compared to select the appropriate substrate in Table 1: loss tangent, areal mass, thickness, and fabrication method.

A rigid-flex substrate is presented in [21] with large array size. This rigid-flex work fabricates many patch antennas on a flexible substrate. By doing so, wide-band antenna design is possible. However, the process variation of the rigid-flex fabrication is too large to realize the Ka-band antenna design. In [22], for a wider bandwidth antenna, an airgap antenna design is adopted. However, this type of fabrication is difficult to realize in Ka-band designs. In [26], an antenna design with a textile as a part of the antenna itself is presented.

TABLE 1. Comparison of rigid and flexible substrates for the deployability.

	This work	Tokyo Tech. IMS2021 [17]	Cal. Tech. Nature El. [18]	Georgia Tech. IMS2022 [24]	MIT EuCAP2020 [21]	FIU OJAP2021 [22]	Georgia Tech. TMTT2020 [26]
Type	Flex	Rigid	Flex	Flex	Rigid-Flex	Rigid-Flex	Flex
Material & structure	4-layer LCP*	5-layer Megtron6	4-layer DuPont^{TM}	2-layer RO4350	2-layer acryl/ 2-layer RO4350	1-layer FR4/ 2-layer Kapton	Polyimide/ Textile
Permittivity, ϵ	2.9	3.4	3.4	3	3.2/3.5	4.4/3.4	1.7**
Loss, $\tan\delta$	0.002	0.004	0.005	0.001	0.003/0.004	0.02/Unknown	0.03**
Application	SATCOM, 5G	SATCOM	RF-WPT	SATCOM, 5G	Unknown	Unknown	Energy Harvesting
Frequency [GHz]	28	24	10	19	10	1.5	32
# of Elements	8×4	4×2	16×16	32	16×16	8×8	1
Integration	ANT[1], AMP[2], PS[3], DIG[4]	ANT, AMP, PS, DIG	ANT, AMP, PS, DIG	ANT, AMP, PS, DIG	ANT	ANT	ANT
Array type	Active phased array	Active phased array	Active phased array	Active phased array	Passive array	Passive array	Single ANT
Areal mass [kg/m^2]	0.96	3.5	1.06	Unknown	1.1	1.1	Unknown
Thickness [mm]	0.9	2	10(stowed) 40(deployed)	0.5	Unknown	50	1.3

* Liquid crystal polymer. ** Two layers are measured together. [1] Antenna. [2] Amplifiers. [3] Phase shifters. [4] Digital controls.

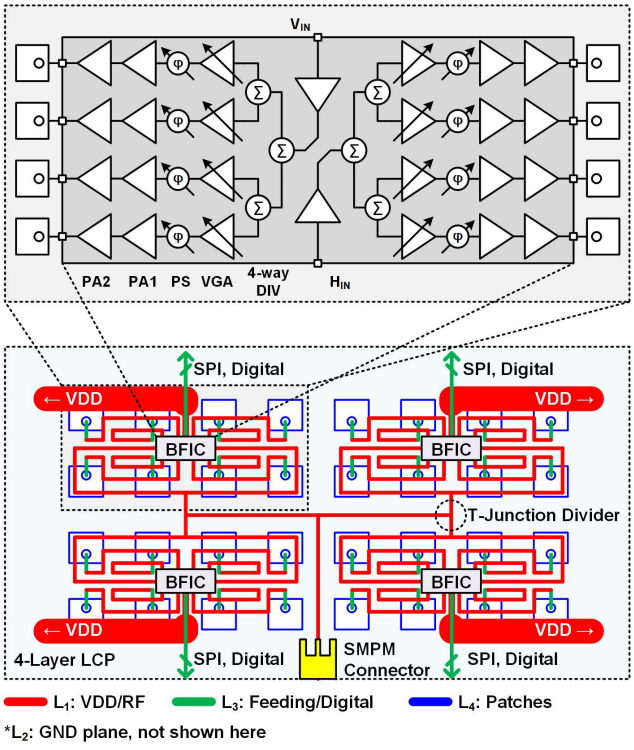

FIGURE 3. System diagram of the proposed active phased array.

While textile-based designs show various usefulness in many applications, variations of the substrate thickness and small form factor antenna design become an issue.

While the above works are not suitable for high integration of an active phased array, the other three works achieved high integrity phased array operation, which requires the integration of BFIC in [17], [18], and [24]. As the easiest fabrication methodology, two rigid boards are connected by coaxial cables via a sub-miniature push-on sub-micro (SMPS) cable and flexible printed cable (FPC) in [17]. While this two-rigid-substrate work achieved high integrity for a 4 × 2 phased array, the loss of substrate is large and the areal mass is too heavy. A 2-layer Rogers flexible substrate is one work with high integrity [24]. This 2-layer Rogers substrate work adopted the inkjet printing technique for ease of fabrication. However, this fabrication method cannot support multi-layer substrates. Because of this reason, while the 2-layer Rogers substrate work achieved a 32-element array size, this methodology is not suitable for the much larger phased arrays. A 4-layer polyimide flexible phased array used in [18] is the most suitable substrate for the proposed deployable active phased-array TX. This 4-layer utilized airgap antennas and discrete patch antennas to overcome high substrate permittivity for better radiation performance of the antenna. Also, the polyimide substrate is highly lossy.

To overcome the aforementioned issues, a 4-layer LCP substrate is adopted in this work. With the 4-layer LCP substrate, complex routing, deployability, stable process variation, low loss, and active phased array integration are achieved.

IV. A PHASED ARRAY DESIGN

The system diagram of the proposed Ka-band active phased-array TX is shown in Fig. 3. To build an active phased array on the limited metal layer substrate, the L_1 layer is used for RF distribution and power supply line, the L_2 layer is for the ground plane, the L_3 layer is for serial peripheral interface (SPI) and other digital control buses, the L_4 layer is for the patch layers. While the RF MSLs are distributed from the center, power supply lines and digital controls are drawn in opposite directions of the RF distribution lines. The proposed phased array TX is composed of 8 × 4 elements. 4 × 2 antennas are driven by a single BFIC in [13]. Four BFICs are used in total for this proof of principle prototype. The BFIC is designed for dual linear polarization, thus it has

two independent RF inputs. On the contrary, this work inputs the same signal from an equally distributed divider as this work is the proof of principle prototype. For a small form factor phased array, a sub-miniature push-on micro (SMPM) connector is mounted at the input of the phased array to drive the TX. Then, the driven signal is divided into eight paths. The eight split paths drive four BFICs. In the following subsections, the design details of the single-element antenna, T-junction divider, SMPM connector signal transition, and array antenna are discussed for the limited metal layer substrate implementation and low-loss design.

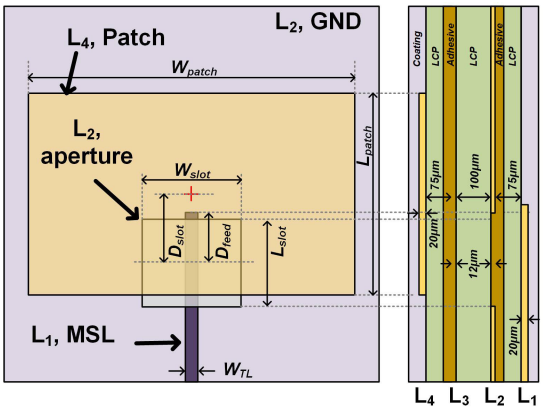

FIGURE 4. A single element antenna design with aperture coupled feeding: top view and lateral view.

TABLE 2. Design parameters of the single-element antenna with aperture-coupled feeding.

W_{TL}	W_{slot}	L_{slot}	D_{slot}	D_{feed}
0.18 mm	1.2 mm	1.4 mm	1.0 mm	0.8 mm
W_{patch}	L_{patch}	Permittivity, ϵ	Loss, $tan\delta$	
4.7 mm	2.9 mm	2.9	0.002	

TABLE 3. Design parameters of the single-element antenna with proximity-coupled feeding.

W_{TL}	W_{feed}	L_{feed}	D_{feed}
0.18 mm	0.5 mm	2.8 mm	0.0 mm
W_{patch}	L_{patch}	Permittivity, ϵ	Loss, $tan\delta$
4.4 mm	2.9 mm	2.9	0.002

A. SINGLE ELEMENTS DESIGN

Element patch antennas are the bulkiest component in a deployable phased-array system because of their thick patch-to-ground-plane height, which is necessary for wide bandwidth, and radiation efficiency. From the antenna design point of view, the substrate is required to be thick vertically. However, if the antenna is too thick, which means the substrate is too thick, the flexibility of the substrate is also

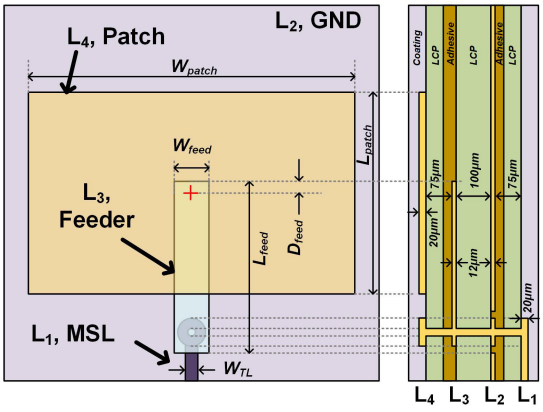

FIGURE 5. A single element antenna design with proximity coupled feeding: top view and lateral view.

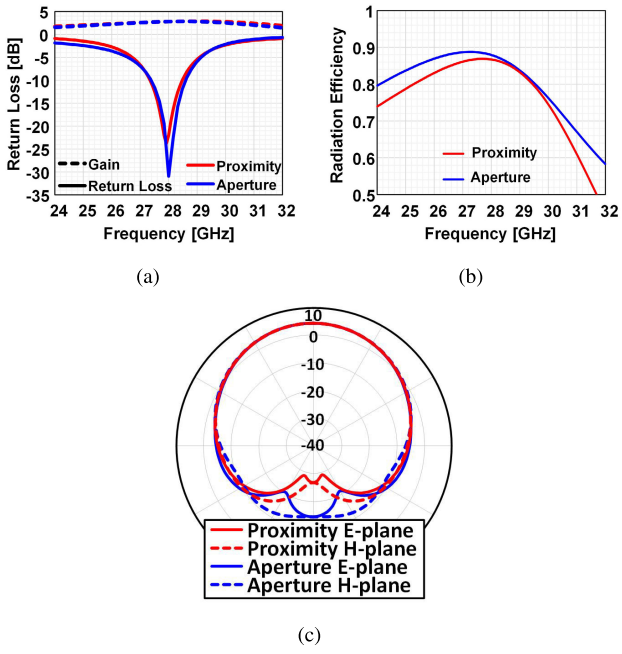

FIGURE 6. Measured and simulated results of the designed single-element antenna: (a) gain, return loss, (b) radiation efficiencies. and (c) radiation patterns.

interrupted. Furthermore, when the array is formed, because of its electrical size (which is nearly half wavelength) and deployment spacing (which is normally half wavelength), all over the substrate is covered by an antenna array. This means that the antenna is bulky not only vertically, but also horizontally. Thus careful low-profile patch antenna design is the critical design consideration in a deployable phased-array system.

In order for increasing the bandwidth under the low patch-to-ground-plane thickness condition, there are many pieces of research about stacked patch antennas, aperture-coupled-fed patch antennas, and proximity-coupled-fed patch antennas for their wideband characteristics [39], [40], [41], [42], [43]. Among bandwidth broadening techniques, the stacked patch

antennas in [39] achieved 57 % of the fractional bandwidth. Nevertheless, it requires an additional patch layer to increase bandwidth, thus techniques requiring bulky structure are not preferred in the deployable phased array design on a flexible substrate. To investigate what feeding technique is superior in the antenna design on a flexible substrate, aperture-coupled feeding, and proximity-coupled feeding methodologies are compared.

Two designed patch antennas with different feeding networks are shown in Fig. 4 and Fig. 5. Their designed parameters are also given in Table. 2 and Table. 3, respectively. To evaluate two antennas, the designed models are simulated with unit cell simulation of the high-frequency structure simulator (HFSS). The results are illustrated in Fig. 6 under the same patch-to-ground thickness, two antennas show similar gain with around 3 dBi and similar bandwidth around 1 GHz defined with -10 dB return loss as shown in Fig. 6(a). The radiation efficiencies of the two different antennas, as depicted in Fig. 6(b), do not exhibit any significant differences, with both antennas achieving an efficiency of 85%. However, the two designs exhibit a big difference in their structure. While the proximity-coupled fed antenna has a small hole in the L_2 ground plane for the via, the aperture-coupled fed antenna has a big aperture in the L_2 ground plane. This huge defect of the L_2 ground plane in the design in Fig. 4 conflicts with the footprint pattern of the BFICs and may invoke unwanted coupling with the L_1 signal routings. As shown in Fig. 6(c), the aperture-coupled fed antenna has 20 dB larger radiation toward the ground plane side. In the conclusion, the proximity-coupled fed antenna is much preferred in antenna design on a flexible substrate than the aperture-coupled fed antenna. Another important design parameter to consider is the error vector magnitude (EVM). Antennas can be affected by thermal noise caused by metal and dielectric losses. However, the impact of antenna-induced noise is usually overshadowed by subsequent active stages. Moreover, since the proposed antenna is utilized in a high-power transmitting system, its contribution to overall noise is relatively insignificant. Therefore, this paper does not include a comparison of EVM between the two antennas.

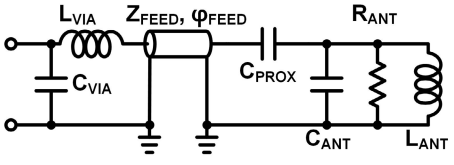

FIGURE 7. Equivalent circuit of the single element antenna design with proximity coupled feeding.

Fig. 7 illustrates an equivalent circuit of the single element antenna with proximity coupled feeding which is adopted in this phased array system. The patch can be modeled as radiation impedance R_{ANT} and L-C resonant tank (L_{ANT}, C_{ANT}). While the simplest proximity-fed patch antennas can be represented with patch L-R-C model and proximity coupling capacitance in series, C_{PROX} as described in [44], the single element antenna in this work has an additional connection: Z_{FEED} Ω and ϕ_{FEED} ° delay transmission line and a via modeled as L_{VIA} and C_{VIA}. This additional connection, naturally, helps to add more degree of freedom in building a matching network while the single proximity coupling capacitance, C_{PROX} gives one-dimensional impedance transformation, thus requiring extra matching networks and extra space.

TABLE 4. Design parameters of the single-element antenna.

W_{TL}	W_{feed}	L_{feed}	D_{feed}
0.18 mm	0.5 mm	2.3 mm	0.5 mm
W_{patch}	L_{patch}	Permittivity, ϵ	Loss, $tan\delta$
4.7 mm	2.9 mm	2.9	0.002

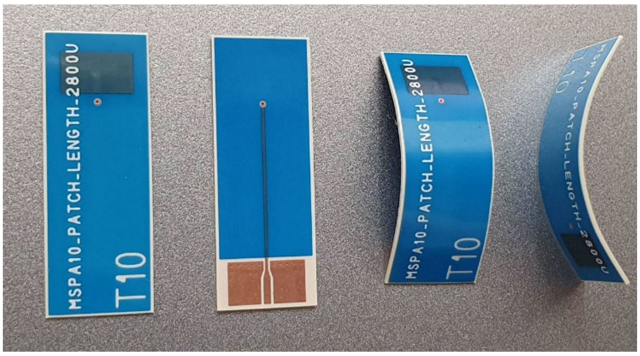

FIGURE 8. Photographs of the fabricated single-element antenna.

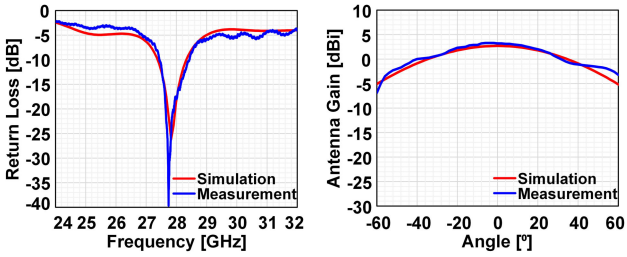

(a) (b)

FIGURE 9. Measured and simulated results of the designed single-element antenna: (a) return loss, (b) antenna gain.

To measure the single-element antenna performance, test element groups (TEG) are fabricated, as shown in Fig. 8. In the TEG fabrication, parameters in Table. 4 are used because there is only a single antenna without adjacent antennas, unlike the array case. In the TEG, SMPM connectors are mounted to drive the antennas through a 10 mm MSL. In order to evaluate the single-element antenna, its return loss, and antenna gain are measured in Fig. 9. Both measured and simulated results in Fig. 9 include an SMPM connector and 10 mm MSL. As illustrated in Fig. 9, the LCP and metal trace model fits real characteristics very well.

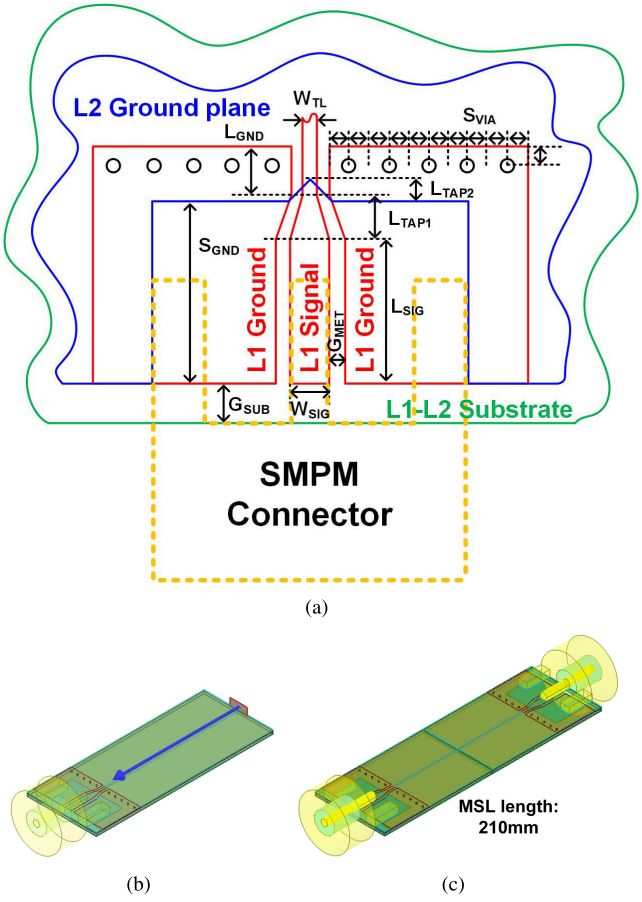

FIGURE 10. Designed (a) coax-to-microstrip pattern with SMPM connector, (b) mm-wave SMPM connector transition 3D model, and (c) 3D model of SMPM connector and 210 mm of the MSL.

TABLE 5. Design parameters of SMPM connector signal transition.

W_{TL}	L_{TAP1}	L_{SIG}	W_{SIG}	G_{MET}
0.18 mm	0.60 mm	1.80 mm	0.50 mm	0.19 mm
G_{SUB}	L_{TAP2}	S_{GND}	L_{GND}	S_{VIA}
0.50 mm	0.30 mm	2.30 mm	0.60 mm	0.25 mm

The measured data reveals that this compact patch antenna design can support large-sized Ka-band deployable active phased-array TXs.

B. MM-WAVE COMPONENTS ON A FLEXIBLE SUBSTRATE

In the large array design, many factors cause large losses, including a coax-to-microstrip transition, long RF distribution lines, transitions of the signal between ICs and a printed circuit board (PCB), and radiation from the PCB. To drive the TX with enough power, even small losses in the paths must be carefully controlled. Especially in the LCP substrate design, because the metal thickness is around half of other rigid substrates, careful low-loss design becomes inevitable.

1) A MM-WAVE SMPM CONNECTOR SIGNAL TRANSITION

To drive the RF signal to the TX from outside the LCP substrate in the deployable array application, an SMPM connector is selected for its small form factor, which helps maintain deployability. Fig. 10(a) shows the designed footprint pattern for the SMPM connector. As illustrated in Fig. 5, the MSL is comprised of a signal line in the L_1 layer, and a ground plane in the L_2 layer. Unlike other rigid substrates, LCP boards have a very thin substrate thickness, which is in the tens of micron level. The thin substrate invokes high inter-layer capacitance between L_1 and L_2 layers. To avoid this parasitic capacitance, a large area of ground pattern in the L_2 layer near the signal pattern in the L_1 is cut. Instead, the impedance of the pattern is controlled by ground patterns in the L_1 layer. Also, to mitigate the abrupt change of the width between the width of the pad of the SMPM connector signal leg and the width of 50 Ω MSL, an appropriate taper is adopted. Furthermore, the vias connecting L_1 and L_2 are deployed far away from the soldering area to avoid air voids that explode in the vacuum environment of space.

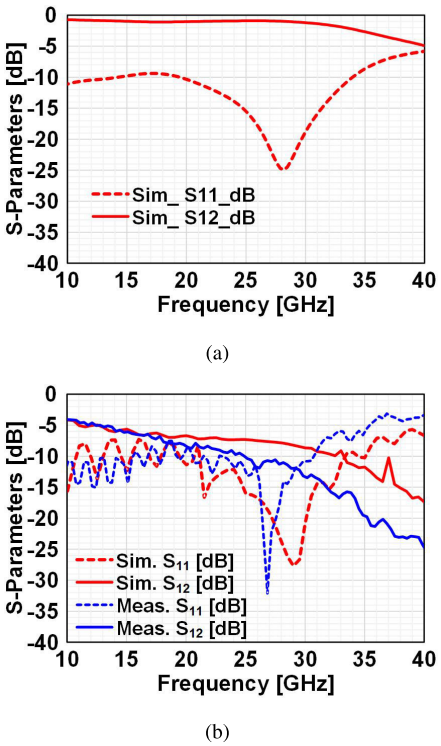

FIGURE 11. (a) Simulated results of the designed SMPM connector transition model, and (b) measured and simulated results of the SMPM connector and 210 mm of the MSL.

To evaluate the designed transition model, the HFSS is used for simulations. The 3D model which includes only the SMPM connector and the coax-to-microstrip transition for the simulation is shown in Fig. 10(b), and the design parameters are summarized in Table. 5. Furthermore, because measuring the transition model at the MSL plane is impossible, a 3D model including two SMPM connectors with

transition patterns, and a 210 mm MSL is created for comparison to the measurement results of the coax-to-microstrip transition TEG. The simulated results for the two 3D models are shown in Fig. 11. As shown in Fig. 11(a), the matching at 28 GHz is well established by controlling the capacitance near the SMPM connector signal leg. This matching curve is also shown for the results of the model in Fig. 10(c) in Fig. 11(b). The measured results of the model in Fig. 10(c) are drawn in Fig. 11(b) and show slight mismatch to the simulated results. However, from a systematic perspective, the such mismatch is negligible.

2) A T-JUNCTION DIVIDER DESIGN

Another important component for the low-loss signal distribution network design in large-size phased arrays is the power divider because a lot of cascaded dividers are required. In this proposed phased-array TX case, there are three cascaded T-junction dividers.

The T-junction divider composes of three 50 Ω port MSLs and two output 70.7 Ω quarter-wavelength MSLs which each have a length of 2.32 mm. The signal pattern is drawn in the L_1 layer, and the L_2 layer is used for the ground plane like the MSLs and the SMPM connector pattern in Fig. 10. The 70.7 Ω MSLs are curved to be fit to a small area so that the designed dividers can be employed in any narrow place. Furthermore, to prepare for a case in which high isolation is required between the two outputs of the divider, the 01005 package size 100 Ω resistor footprint at the output of the 70.7 Ω MSLs is drawn as well. The copper pattern of the designed T-junction divider and the 3D model of the designed divider for the electromagnetic simulation are illustrated in Fig. 12(a) and Fig. 12(b), respectively. The design parameters of the T-junction divider are summarized in Table. 6.

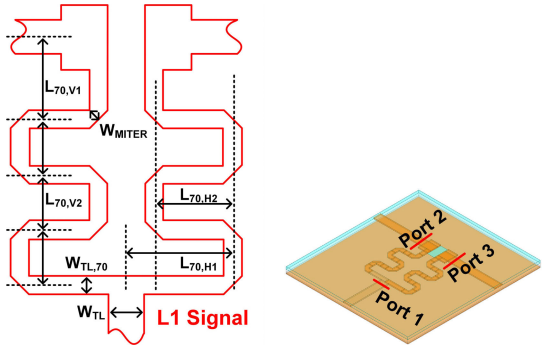

FIGURE 12. Designed (a)mm-wave divider parameters, and (b) divider 3D model.

The simulated S-parameters of the designed T-junction divider are displayed in Fig. 13. The magnitude of S_{21} is −3.28 dB, thus the simulated loss is 0.27 dB. The real loss is expected to be slightly larger than 0.27 dB because the substrate loss model is underestimated as depicted in the data in Fig. 11(b). However, frequency characteristics including matching, S_{11} in Fig. 13 are expected to be quite well matched

TABLE 6. Design parameters of T-junction divider.

W_{TL}	$W_{TL,70}$	W_{MITER}	
0.18 mm	0.08 mm	0.04 mm	
$L_{70,H1}$	$L_{70,H2}$	$L_{70,V1}$	$L_{70,V2}$
0.46 mm	0.26 mm	0.36 mm	0.24 mm

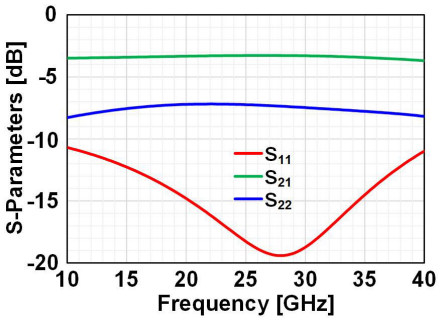

FIGURE 13. Simulated results of the designed divider.

at the center frequency of 28 GHz because the 3D substrate model is well fitted as shown in Fig. 9 and Fig. 11.

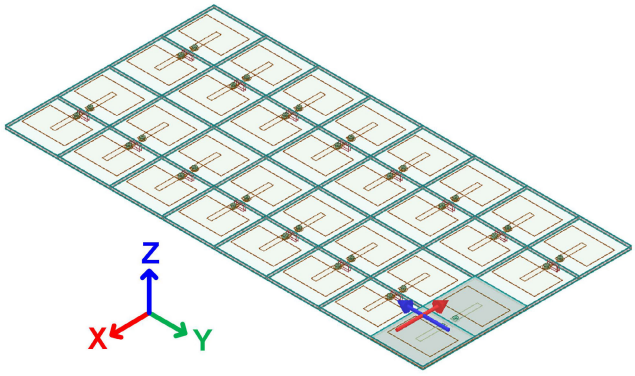

FIGURE 14. Finite array domain decomposition method 3D model of the designed array antenna.

C. ARRAY DESIGN

In order for an elaborated array design, a 3D model of the 8 × 4-element array antenna is built and simulated using Finite Array Domain Decomposition Method (HFSS) in the HFSS as illustrated in Fig. 14. For the periodic layout of the output distribution lines after the BFICs, two rows of antennas are deployed in a back-to-back arrangement. This back-to-back deployment shifts the phase between the upper and the lower rows of the antennas by 180°. That the 180° phase shift is compensated by a 180° phase shift in BFIC.

Because each element antenna cannot be isolated from the ground via a fence or a ground ring pattern in layer L_4 due to the low substrate thickness and lack of the number of metal layers, the inter-element coupling is not negligible, thus the matching also slightly changes. Based on the array

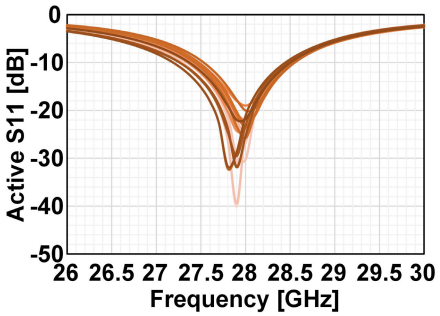

(a)

Freq.: 27~29GHz

(b)

FIGURE 15. Simulated active S-parameters of 8 × 4 elements in (a) cartesian coordinate, and (b) smith chart.

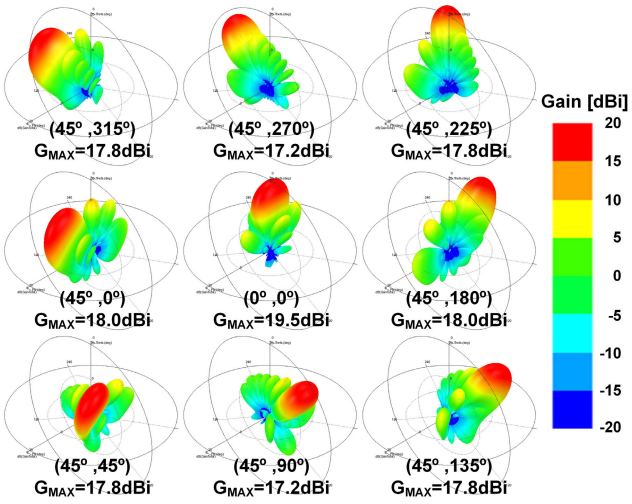

FIGURE 16. Simulated 3D beam patterns of the designed 8 × 4 array with different beam steering states (θ, ϕ).

composition, antenna ports are re-matched, and their results are in Fig. 15 using the 3D model in Fig. 14. The modified model parameters are re-summarized in Table. 3. As illustrated in Fig. 15(a), a 1 GHz of bandwidth is defined with the active S-parameters.

Not only are the active S-parameters but the 3D beam patterns are also simulated in Fig. 16 to investigate the designed phased array in more detail. As given in the Fig. 16, 19.5 dBi, 18.0 dBi, 17.2 dBi of antenna gains are achieved at $(\theta, \phi) = (0°, 0°)$, $(\theta, \phi) = (45°, 0°)$, $(\theta, \phi) = (45°, 90°)$, respectively.

V. ARRAY IMPLEMENTATION AND EMPIRICAL RESULTS

Fig. 17 shows the front-side view, the back-side view, the bent shape, and the measured weight of the fabricated 8 × 4-element deployable phased-array TX. On the front side, four BFICs are soldered with a wafer-level chip scale package (WLCSP). Antennas are built on the back side of the LCP substrate. For better periodicity in the antenna array, one row of antennas are surrounding the fed antenna array. Antennas are spaced by 5.4 mm, which is a half wavelength at 28 GHz. An SMPM connector for the RF signal drive is soldered for a small form factor phased array. As depicted in Fig. 17, the proposed deployable phased-array TX on the LCP substrate achieved an extremely lightweight of 2.49 g. As this work is a proof of principle prototype, creases are not yet formed. Also, unlike SATCOM TXs, the circular polarization feature is not implemented yet. The circular polarization and creases will be implemented in the 32 × 32-element phased-array TX as the MTT-Sat Challenge progresses.

To evaluate the proposed deployable active phased-array TX on the LCP substrate, beam patterns at various beam angle modes are measured. The test bench for the beam pattern measurement is shown in Fig. 18. A Keysight E8257D signal generator drives the device-under-test (DUT) with a 28GHz RF signal. After the DUT controls the beam angle, at 0.7 m away, a commercial off-the-self horn antenna receives the RF signal. The received RF signal is then directly sampled by a Keysight E4448A spectrum analyzer.

The measured beam pattern results are illustrated in Fig. 19. 4 × 4 elements are activated in this measurement. Even without any phased array element calibration, the main lobe of the measured results fits well with the simulated results in Fig. 19(a). While the measured side lobes slightly differ from the simulated side lobes, the side lobe level (SLL) is well suppressed by more than 10 dB. Steered beam patterns at −50°, −40°, −20°, 0°, 20°, 40°, 50° are evaluated as well in Fig. 19(b). Fig. 19(b) reveals that the proposed deployable active phased-array TX on the LCP substrate can control the beam direction cleanly.

For further evaluation of the proposed deployable active phased-array TX on the LCP substrate, in Fig. 20, EVM of the DVB-S2 modulated signal through TX passes are measured as well. The modulated signals at 4 GHz intermediate frequency (IF) are generated in the Keysight M8195A arbitrary waveform generator (AWG). The generated IF is then upconverted to a 28 GHz RF signal by a 24 GHz local oscillation signal, which is generated by the Keysight E8257D signal generator. The upconverted RF signal is driven to the DUT. At 0.4 m away, the commercial off-the-self horn antenna receives the RF signal. The received signal is then directly sampled and demodulated by the Keysight UXR0254 oscilloscope. The oscilloscope has a 256 GHz real-time sampling rate and can downconvert the RF signal using a digital

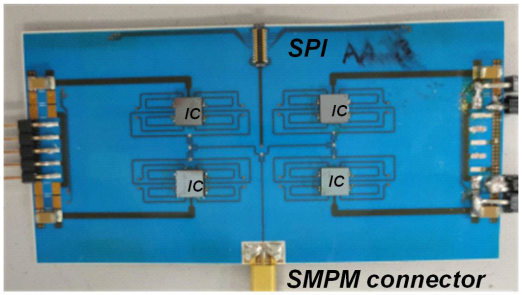

(a)

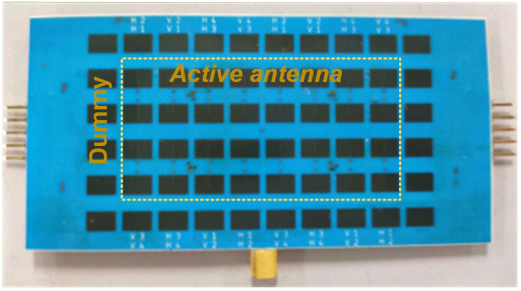

(b)

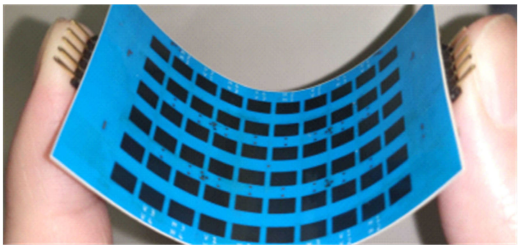

(c)

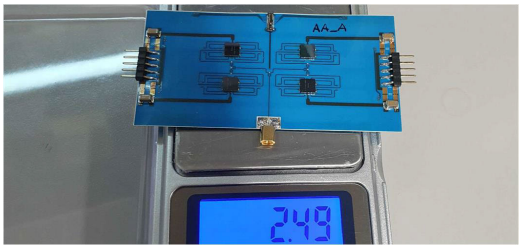

(d)

FIGURE 17. Fabricated deployable phased-array TX: (a) front-side view, (b) back-side view, (c) bent board view, and (d) measured weight.

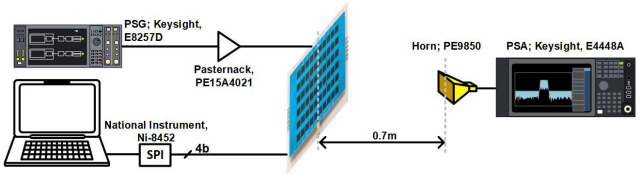

FIGURE 18. Measurement setup for beam patterns.

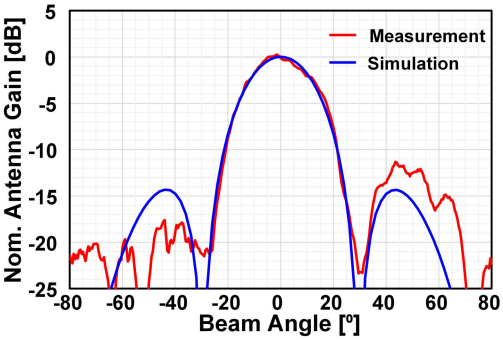

(a)

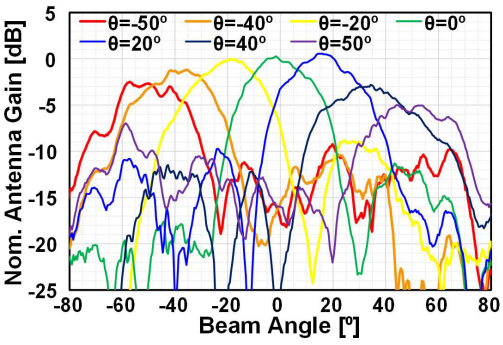

(b)

FIGURE 19. Beam patterns: (a) at 0° beam angle by simulation and measurement, (b) at various beam angles by measurement.

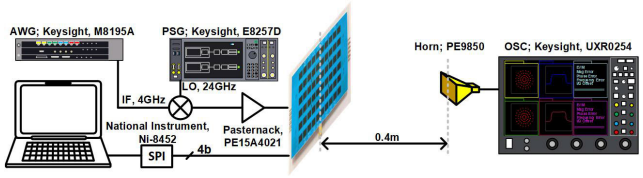

FIGURE 20. Measurement setup for over-the-air EVM with DVB-S2 modulated signals.

Modulation	16 APSK	32 APSK	16 APSK	32 APSK
Constellation	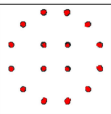	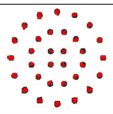	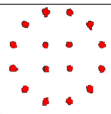	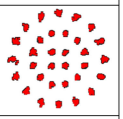
Symbol rate [MS/s]	100	100	500	500
Data rate [Gbps]	0.4	0.5	2	2.5
EVM [dB]	-33.0	-32.4	-29.7	-28.7

FIGURE 21. Measured constellations and EVM with DVB-S2 signals.

downconversion mixer, which makes the measurement setup far simpler.

Fig. 21 shows measured constellation and EVM results with the DVB-S2 standard signal, 16-APSK, and 32-APSK modulation. In the measurement, 4 × 2 elements with a single BFIC are utilized at 6 dBm output power of a single PA, which is 10 dB back-off from the saturated power level. Under 100 MBaud and 32-APSK signal conditions, −32.4 dB EVM is achieved. With 500 MBaud sybmbolrate, −28.7 dB EVM is achieved at a 6 dBm output power. From

this measurement setup, 2.5 Gbps of the data rate is achieved with the 500 MBaud and 32-APSK modulation conditions.

VI. CONCLUSION

A proof of principle prototype of Ka-band 8 × 4-element deployable phased-array TX with the proposed 4-layer LCP substrate structure is presented for future space demonstration with a 32 × 32-element phased-array TX as being supported by MTT-Sat Challenge. The detailed designs for the phased-array TX RF components are presented as well. The RF components are designed with low loss characteristics against the low metal thickness of the LCP board and long signal distribution lines for the big array size. The presented deployable phased-array TX with the LCP substrate can steer the beam from −50° to 50°. The phased-array TX can drive 32-APSK DVB-S2 signal at 6 dBm single PA output power level with the −28.7 dB EVM. The proposed deployable phased-array TX achieved the lightest and thinnest deployable active phased-array with 0.96 kg/m^2 areal mass, and 0.9 mm thickness. In summary, this paper provided a new class of Ka-band deployable active phased-array TXs for Small-Satellite to expedite future low-earth orbit satellite communication.

REFERENCES

[1] X. Liu, K. Lam, F. Li, J. Zhao, L. Wang, and T. S. Durrani, "Spectrum sharing for 6G integrated satellite-terrestrial communication networks based on NOMA and CR," *IEEE Netw.*, vol. 35, no. 4, pp. 28–34, Jul. 2021.

[2] A. Shirane, Y. Wang, and K. Okada, "A CMOS Ka-band wireless transceiver for future non-terrestrial 6G networks," in *Proc. IEEE 15th Int. Conf. Solid-State Integr. Circuit Technol. (ICSICT)*, Nov. 2020, pp. 1–3.

[3] E. Juan, M. Lauridsen, J. Wigard, and P. E. Mogensen, "5G new radio mobility performance in LEO-based non-terrestrial networks," in *Proc. IEEE Globecom Workshops (GC Wkshps*, Dec. 2020, pp. 1–6.

[4] D. You, Y. Wang, X. Fu, H. Herdian, X. Wang, A. Fadila, H. Lee, M. Ide, S. Kato, Z. Li, J. Pang, A. Shirane, and K. Okada, "A Ka-band dual circularly polarized CMOS transmitter with adaptive scan impedance tuner and active XPD calibration technique for satellite terminal," in *Proc. IEEE Radio Freq. Integr. Circuits Symp. (RFIC)*, Jun. 2022, pp. 15–18.

[5] J. Ylitalo, *Hybrid Satellite Systems: Extending Terrestrial Networks Using Satellites*. Amsterdam, The Netherlands: Elsevier, 2015, doi: 10.1016/B978-0-12-799948-7.00011-6.

[6] B. Sadhu, A. Paidimarri, W. Lee, M. Yeck, C. Ozdag, Y. Tojo, J. Plouchart, X. Gu, Y. Uemichi, S. Chakraborty, Y. Yamaguchi, N. Guan, and A. Valdes-Garcia, "A 24-to-30G Hz 256-element dual-polarized 5G phased array with fast beam-switching support for >30,000 beams," in *Proc. IEEE Int. Solid- State Circuits Conf. (ISSCC)*, vol. 65, Feb. 2022, pp. 436–438.

[7] Z. Li, J. Pang, Y. Zhang, Y. Yamazaki, Q. Wang, P. Luo, W. Chen, Y. Liao, M. Tang, Z. Guo, Y. Wang, X. Fu, D. You, N. Oshima, S. Hori, K. Kunihiro, A. Shirane, and K. Okada, "A 39-GHz CMOS bi-directional Doherty phased-array beamformer using shared-LUT DPD with inter-element mismatch compensation technique for 5G base-station," in *Proc. IEEE Symp. VLSI Technol. Circuits (VLSI Technol. Circuits)*, Jun. 2022, pp. 98–99.

[8] Y. Yin, S. Zihir, T. Kanar, Q. Ma, H. Chung, L. Gao, and G. M. Rebeiz, "A 37–42-GHz 8 × 8 phased-array with 48–51-dBm EIRP, 64–QAM 30-Gb/s data rates, and EVM analysis versus channel RMS errors," *IEEE Trans. Microw. Theory Techn.*, vol. 68, no. 11, pp. 4753–4764, Nov. 2020.

[9] H. Kim, B. Park, S. Song, T. Moon, S. Kim, J. Kim, J. Chang, and Y. Ho, "A 28-GHz CMOS direct conversion transceiver with packaged 2 × 4 antenna array for 5G cellular system," *IEEE J. Solid-State Circuits*, vol. 53, no. 5, pp. 1245–1259, May 2018.

[10] K. Kibaroglu, M. Sayginer, and G. M. Rebeiz, "A low-cost scalable 32-element 28-GHz phased array transceiver for 5G communication links based on a 2 × 2 beamformer flip-chip unit cell," *IEEE J. Solid-State Circuits*, vol. 53, no. 5, pp. 1260–1274, May 2018.

[11] H.-C. Park, D. Kang, S. Lee, B. Park, K. Kim, J. Lee, Y. Aoki, Y. Yoon, S. Lee, and D. Lee, "4.1 A 39 GHz-band CMOS 16-channel phased-array transceiver IC with a companion dual-stream IF transceiver IC for 5G NR base-station applications," in *Proc. IEEE Int. Solid- State Circuits Conf. (ISSCC)*, Feb. 2020, pp. 76–78.

[12] Y. Wang, "A 39-GHz 64-element phased-array transceiver with built-in phase and amplitude calibrations for large-array 5G NR in 65-nm CMOS," *IEEE J. Solid-State Circuits*, vol. 55, no. 5, pp. 1249–1269, May 2020.

[13] J. Pang, Z. Li, X. Luo, J. Alvin, R. Saengchan, A. A. Fadila, K. Yanagisawa, Y. Zhang, Z. Chen, and Z. Huang, "A CMOS dual-polarized phased-array beamformer utilizing cross-polarization leakage cancellation for 5G MIMO systems," *IEEE J. Solid-State Circuits*, vol. 56, no. 4, pp. 1310–1326, Apr. 2021.

[14] A. Nafe, M. Sayginer, K. Kibaroglu, and G. M. Rebeiz, "2 × 64-element dual-polarized dual-beam single-aperture 28-GHz phased array with 2 × 30 Gb/s links for 5G polarization MIMO," *IEEE Trans. Microw. Theory Techn.*, vol. 68, no. 9, pp. 3872–3884, Sep. 2020.

[15] J. Park, S. Lee, J. Chun, L. Jeon, and S. Hong, "A 28-GHz four-channel beamforming front-end IC with dual-vector variable gain phase shifters for 64-element phased array antenna module," *IEEE J. Solid-State Circuits*, vol. 58, no. 4, pp. 1142–1159, Apr. 2023.

[16] A. C. Fikes, M. Gal-Katziri, O. S. Mizrahi, D. E. Williams, and A. Hajimiri, "Frontiers in flexible and shape-changing arrays," *IEEE J. Microw.*, vol. 3, no. 1, pp. 349–367, Jan. 2023.

[17] D. You, Y. Takahashi, S. Takeda, M. Moritani, H. Hagiwara, S. Koike, H. Lee, Y. Wang, Z. Li, J. Pang, A. Shirane, H. Sakamoto, and K. Okada, "A Ka-band 16-element deployable active phased array transmitter for satellite communication," in *IEEE MTT-S Int. Microw. Symp. Dig.*, Jun. 2021, pp. 799–802.

[18] M. Gal-Katziri, A. Fikes, and A. Hajimiri, "Flexible active antenna arrays," *NPJ Flexible Electron.*, vol. 6, no. 1, p. 85, Oct. 2022, doi: 10.1038/s41528-022-00218-z.

[19] A. Fikes, O. S. Mizrahi, and A. Hajimiri, "A framework for array shape reconstruction through mutual coupling," *IEEE Trans. Microw. Theory Techn.*, vol. 69, no. 10, pp. 4422–4436, Oct. 2021.

[20] A. C. Fikes, A. Safaripour, F. Bohn, B. Abiri, and A. Hajimiri, "Flexible, conformal phased arrays with dynamic array shape self-calibration," in *IEEE MTT-S Int. Microw. Symp. Dig.*, Jun. 2019, pp. 1458–1461.

[21] W. F. Moulder, R. N. Das, A. C. Maccabe, L. A. Bowen, E. M. Thompson, and P. J. Bell, "Rigid-flexible antenna array (RFAA) for lightweight deployable apertures," in *Proc. 14th Eur. Conf. Antennas Propag. (EuCAP)*, Mar. 2020, pp. 1–5.

[22] M. Carvalho and J. L. Volakis, "Deployable rigid-flexible tightly coupled dipole array (RF-TCDA)," *IEEE Open J. Antennas Propag.*, vol. 2, pp. 1184–1193, 2021.

[23] J. A. Caripidis Troccola, M. Carvalho, M. R. Islam, and J. L. Volakis, "Deployable tightly coupled dipole reflectarray for small satellites," in *Proc. IEEE Int. Symp. Antennas Propag. USNC-URSI Radio Sci. Meeting (AP-S/URSI)*, Jul. 2022, pp. 163–164.

[24] K. Hu, G. Soto-Valle, Y. Cui, and M. M. Tentzeris, "Flexible and scalable additively manufactured tile-based phased arrays for satellite communication and 50 mm wave applications," in *IEEE MTT-S Int. Microw. Symp. Dig.*, Jun. 2022, pp. 691–694.

[25] X. He and M. M. Tentzeris, "In-package additively manufactured sensors for bend prediction and calibration of flexible phased arrays and flexible hybrid electronics," in *IEEE MTT-S Int. Microw. Symp. Dig.*, Jun. 2021, pp. 327–330.

[26] M. Wagih, G. S. Hilton, A. S. Weddell, and S. Beeby, "Broadband millimeter-wave textile-based flexible rectenna for wearable energy harvesting," *IEEE Trans. Microw. Theory Techn.*, vol. 68, no. 11, pp. 4960–4972, Nov. 2020.

[27] S. Adami, P. Proynov, G. S. Hilton, G. Yang, C. Zhang, D. Zhu, Y. Li, S. P. Beeby, I. J. Craddock, and B. H. Stark, "A flexible 2.45-GHz power harvesting wristband with net system output from -24.3 dBm of RF power," *IEEE Trans. Microw. Theory Techn.*, vol. 66, no. 1, pp. 380–395, Jan. 2018.

[28] X. Wang, D. You, X. Fu, H. Lee, Z. Li, D. Awaji, J. Pang, A. Shirane, H. Sakamoto, and K. Okada, "A flexible implementation of Ka-band active phased array for satellite communication," in *Proc. IEEE/MTT-S Int. Microw. Symp.*, Jun. 2022, pp. 753–756.

[29] D. You, D. Awaji, A. Shirane, H. Sakamoto, and K. Okada, "A flexible element antenna for Ka-band active phased array SATCOM transceiver," in *Proc. IEEE Asia–Pacific Microw. Conf. (APMC)*, Dec. 2020, pp. 991–993.

[30] K. Ikeyal, "Significance of 3U CubeSat OrigamiSat-1 for space demonstration of multifunctional deployable membrane," *Acta Astronautica*, vol. 173, pp. 363–377, Aug. 2020. [Online]. Available: https://www.sciencedirect.com/science/article/pii/S0094576520302204
[31] T. Chen, O. R. Bilal, R. Lang, C. Daraio, and K. Shea, "Autonomous deployment of a solar panel using elastic origami and distributed shape-memory-polymer actuators," *Phys. Rev. Appl.*, vol. 11, no. 6, Jun. 2019, Art. no. 064069. [Online]. Available: https://link.aps.org/doi/10.1103/PhysRevApplied.11.064069
[32] R. J. Lang, S. Magleby, and L. Howell, "Single degree-of-freedom rigidly foldable cut origami flashers," *J. Mech. Robot.*, vol. 8, no. 3, Jun. 2016, Art. no. 031005, doi: 10.1115/1.4032102.
[33] S. A. Zirbel, R. J. Lang, M. W. Thomson, D. A. Sigel, P. E. Walkemeyer, B. P. Trease, S. P. Magleby, and L. L. Howell, "Accommodating thickness in origami-based deployable arrays1," *J. Mech. Design*, vol. 135, no. 11, Nov. 2013, Art. no. 111005, doi: 10.1115/1.4025372.
[34] "Propagation data and prediction methods required for the design of earth-space telecommunication systems," Int. Telecommun. Union (ITU), Geneva, Switzerland, Tech. Rep. P.618-13, Dec. 2017. [Online]. Available: https://www.itu.int/rec/R-REC-P.618/
[35] "Characteristics of precipitation for propagation modeling," Int. Telecommun. Union (ITU), Geneva, Switzerland, Tech. Rep. P.837-7, Jun. 2017. [Online]. Available: https://www.itu.int/rec/R-REC-P.837
[36] "Specific attenuation model for rain for use in prediction methods," Int. Telecommun. Union (ITU), Geneva, Switzerland, Tech. Rep. P.838-3, Mar. 2005. [Online]. Available: https://www.itu.int/rec/R-REC-P.838
[37] "Rain height model for prediction methods," Int. Telecommun. Union (ITU), Geneva, Switzerland, Tech. Rep. P.839-4, Sep. 2013. [Online]. Available: https://www.itu.int/rec/R-REC-P.839
[38] "Rain height model for prediction methods," Int. Telecommun. Union (ITU), Geneva, Switzerland, Tech. Rep. P.1511-2, Aug. 2019. [Online]. Available: https://www.itu.int/rec/R-REC-P.1511
[39] M. A. Matin, B. S. Sharif, and C. C. Tsimenidis, "Probe fed stacked patch antenna for wideband applications," *IEEE Trans. Antennas Propag.*, vol. 55, no. 8, pp. 2385–2388, Aug. 2007.
[40] X. Tong, Z. H. Jiang, C. Yu, F. Wu, X. Xu, and W. Hong, "Low-profile, broadband, dual-linearly polarized, and wide-angle millimeter-wave antenna arrays for Ka-band 5G applications," *IEEE Antennas Wireless Propag. Lett.*, vol. 20, no. 10, pp. 2038–2042, Oct. 2021.
[41] S. K. Padhi, N. C. Karmakar, C. L. Law, and S. Aditya, "A dual polarized aperture coupled circular patch antenna using a c-shaped coupling slot," *IEEE Trans. Antennas Propag.*, vol. 51, no. 12, pp. 3295–3298, Dec. 2003.
[42] S. Gao, L. W. Li, M. S. Leong, and T. S. Yeo, "A broad-band dual-polarized microstrip patch antenna with aperture coupling," *IEEE Trans. Antennas Propag.*, vol. 51, no. 4, pp. 898–900, Apr. 2003.
[43] A. Jafargholi, M. Kamyab, M. Veysi, and M. N. Azar, "Microstrip gap proximity fed-patch antennas, analysis, and design," *AEU Int. J. Electron. Commun.*, vol. 66, no. 2, pp. 115–121, Feb. 2012. [Online]. Available: https://www.sciencedirect.com/science/article/pii/S1434841111001695
[44] R. Garg, P. Bhartia, I. Bahl, and A. Ittipiboon, *Microstrip Antenna Design Handbook*, 1st ed. Norwood, MA, USA: Artech House, 2001.

DONGWON YOU (Graduate Student Member, IEEE) received the B.S. degree in electrical and computer engineering from Ajou University, Suwon, South Korea, in 2017, and the M.S. degree in electrical and electronic engineering from the Tokyo Institute of Technology (Tokyo Tech), Tokyo, Japan, in 2019, where he is currently pursuing the Ph.D. degree in electrical and electronic engineering.

His current research interests include CMOS RF/millimeter-wave/analog transceiver systems, MIMO, mixed-signal, wireless communication, device modeling, and satellite communication. He was a recipient of the IEEE SSCS Student Travel Grant Award, in 2022, the Best Student Paper Award (First Place) from the 2019 IEEE Radio Frequency Integrated Circuits Symposium (RFIC), and the IEEE Microwave Theory and Techniques Society MTT-Sat Challenge Phase1, Phase2, Phase3. He serves as a Reviewer for the IEEE JOURNAL OF SOLID-STATE CIRCUITS, IEEE TRANSACTIONS ON MICROWAVE THEORY AND TECHNIQUES, and *IEEE Microwave Magazine*.

XIAOLIN WANG (Student Member, IEEE) received the B.E. degree in electrical engineering from the University of Electronic Science and Technology of China, Chengdu, China, in 2020, and the M.E. degree from the Tokyo Institute of Technology, Tokyo, Japan, where he is currently pursuing the Ph.D. degree. His research interests include CMOS millimeter-wave transceivers, satellite communication, and phased-array transceiver.

HANS HERDIAN (Member, IEEE) was born in Bekasi, Indonesia. He received the B.Sc. degree from the Bandung Institute of Technology, Bandung, Indonesia, in 2016, and the M.S. degree from the Tokyo Institute of Technology, Tokyo, Japan, in 2018, where he is currently pursuing the Ph.D. degree. His research interests include passive components characterization and performance enhancement on CMOS process for mm-wave application.

XI FU (Graduate Student Member, IEEE) received the B.E. degree (Hons.) from the Dalian University of Technology, Liaoning, China, in 2017, and the M.E. and Ph.D. degrees from the Department of Electrical and Electronic Engineering, Tokyo Institute of Technology, Tokyo, Japan, in 2019 and 2022, respectively.

He is currently a Postdoctoral Researcher with the Tokyo Institute of Technology. His research interests include CMOS radio frequency (RF)/millimeter-wave/terahertz transceivers, phased-array transceivers, mixed-signal systems, 5G mobile systems, and satellite communication systems.

Dr. Fu was a recipient of the Japanese Government [the Ministry of Education, Culture, Sports, Science, and Technology of Japan (MEXT)] Scholarship, the RF Integrated Circuits (RFIC) Symposium Best Paper Award, the International Solid-State Circuits Conference (ISSCC) Student-Research Preview Poster Award, in 2022, and the IEEE Solid-State Circuits Society (SSCS) Student Travel Grant Award, in 2022. He serves as a Reviewer for the IEEE TRANSACTIONS ON MICROWAVE THEORY AND TECHNIQUES and the IEEE TRANSACTIONS ON CIRCUITS AND SYSTEMS—I: REGULAR PAPERS.

HOJUN LEE was born in Daejeon, South Korea. He received the B.Sc. degree from the Department of Electrical and Electronic Engineering, Tokyo Institute of Technology, in 2020, where he is currently pursuing the M.S. degree. His research interests include phased array transceivers and wireless power transmission.

MICHIHIRO IDE (Graduate Student Member, IEEE) received the B.E. and M.E. degrees in electrical and electronic engineering from the Tokyo Institute of Technology, Tokyo, Japan, in 2020 and 2022, respectively, where he is currently pursuing the Ph.D. degree in electrical and electronic engineering. His current research interests include CMOS millimeter-wave and sub-terahertz integrated circuit for wireless communication, phased-array transceiver, low-power wireless communication system for the IoT, and wireless power transfer systems.

CARREL DA GOMEZ (Graduate Student Member, IEEE) received the B.Sc. degree in electrical engineering from the Institut Teknologi Bandung, Bandung, Indonesia, in 2017, and the M.Eng. degree in electrical and electronic engineering from the Tokyo Institute of Technology, Tokyo, Japan, in 2020, where he is currently pursuing the Ph.D. degree in electrical and electronic engineering. His current research interests include CMOS millimeter-wave and sub-terahertz integrated circuits for wireless communication and radar. He was a recipient of the Japanese Government (MEXT) Scholarship, in 2018.

ZHENG LI (Graduate Student Member, IEEE) received the B.E. and M.E. degrees in microelectronics and solid electronics from Xidian University, Xi'an, China, in 2014 and 2017, respectively. He is currently pursuing the Ph.D. degree in electrical and electronic engineering with the Tokyo Institute of Technology, Tokyo, Japan, with a focus on the fifth-generation (5G) and beyond-5G wireless communication system design.

His research interests include radio frequency (RF)/millimeter-wave CMOS phased-array beamformers, 5G area-power-efficient power amplifiers (PAs), and 5G high-data rate mobile systems.

JILL MAYEDA (Member, IEEE) received the B.Sc. degree in applied and computational mathematical sciences from the University of Washington, Seattle, WA, USA, in 2014, and the Ph.D. degree in electrical engineering from Texas Tech University, Lubbock, TX, USA, in 2022. She has spent seven years in industry by working at Noise Figure Research, from 2015 to 2022. She is currently a Postdoctoral Researcher with the Tokyo Institute of Technology, Tokyo, Japan, with a research focus on CMOS satellite communication transceivers. Her research interests include mm-wave PA design using CMOS, HBT, and III-V technologies, and CMOS mm-wave transceiver design. She received the Best Ph.D. Student Award from Texas Tech University, in 2022.

DAISUKE AWAJI received the B.E. and M.E. degrees from the University of Utsunomiya, Japan in 2005 and 2007, respectively. Since 2007, he has been with Fujikura Ltd., where he was involved in optical sensor, fiber laser, and optical and electronic wireless communication technologies. Since 2015, he has also been engaged in advanced substrate technologies for millimeter-wave communication devices. His current research interest includes the design and development of multilayer antenna board with low dielectric materials.

JIAN PANG (Member, IEEE) received the bachelor's and master's degrees from Southeast University, Nanjing, China, in 2012 and 2014, respectively, and the Ph.D. degree from the Department of Physical Electronics, Tokyo Institute of Technology, Tokyo, Japan, in 2019.

From 2019 to 2020, he was a Postdoctoral Researcher with the Tokyo Institute of Technology. From 2020 to 2022, he was a Special-Appointed Assistant Professor with the Tokyo Institute of Technology, where he is currently a Special-Appointed Associated Professor, focusing on 5G millimeter-wave systems. His research interests include high-data-rate low-cost millimeter-wave transceivers, power-efficient power amplifiers (PAs) for 5G mobile systems, multiple-in–multiple out (MIMO), and mixed-signal calibration systems.

Dr. Pang was a recipient of the IEEE Solid-State Circuits Society (SSCS) Student Travel Grant Award, in 2016, the IEEE SSCS Pre-Doctoral Achievement Award for the term 2018–2019, the Seiichi Tejima Oversea Student Research Award, in 2020, and the IEEE Microwave Theory and Techniques Society (MTT-S) Japan Young Engineer Award, in 2021.

HIRAKU SAKAMOTO received the Ph.D. degree in aerospace engineering sciences from the University of Colorado at Boulder, Boulder, CO, USA. He is currently an Associate Professor with the Department of Mechanical Engineering, Tokyo Institute of Technology (Tokyo Tech), Japan. From 2019 to 2020, he was a Visiting Scholar with Aalto University, Finland, hosted by the Space Technology Group, Department of Electronics and Nanoengineering. He has been a principal investigator of two 3U CubeSats, OrigamiSat-1, and OrigamiSat-2, mainly developed at Tokyo Tech.

KENICHI OKADA (Fellow, IEEE) received the B.E., M.E., and Ph.D. degrees in communications and computer engineering from Kyoto University, Kyoto, Japan, in 1998, 2000, and 2003, respectively.

From 2000 to 2003, he was a Research Fellow with the Japan Society for the Promotion of Science, Kyoto University. In 2003, he joined the Tokyo Institute of Technology, Tokyo, Japan, as an Assistant Professor, where he is currently a Professor of electrical and electronic engineering. He has authored or coauthored more than 500 journal and conference papers. His current research interests include millimeter-wave and terahertz CMOS wireless transceivers for 20/28/39/60/77/79/100/300 GHz for 5G, WiGig, satellite and future wireless systems, digital PLL, synthesizable PLL, atomic clock, and ultra-low-power wireless transceivers for Bluetooth low-energy, and sub-GHz applications.

Prof. Okada is a member of the Institute of Electronics, Information and Communication Engineers (IEICE), the Information Processing Society of Japan (IPSJ), and the Japan Society of Applied Physics (JSAP). He was a recipient or co-recipient of the Ericsson Young Scientist Award, in 2004, the A-SSCC Outstanding Design Award, in 2006 and 2011, the ASP-DAC Special Feature Award, in 2011, the Best Design Award, in 2014 and 2015, the MEXT Young Scientists' Prize in 2011, the JSPS Prize in 2014, the Suematsu Yasuharu Award, in 2015, the MEXT Prizes for Science and Technology, in 2017, the RFIT Best Paper Award, in 2017, the IEICE Best Paper Award, in 2018, the RFIC Symposium Best Student Paper Award, in 2019, the IEICE Achievement Award, in 2019, the DOCOMO Mobile Science Award, in 2019, the IEEE/ACM ASP-DAC Prolific Author Award, in 2020, the Kenjiro Takayanagi Achievement Award, in 2020, the KDDI Foundation Award, in 2020, the IEEE CICC Best Paper Award, in 2020, and more than 50 other international and domestic awards. He is/was a member of the technical program committees of the IEEE International Solid-State Circuits Conference (ISSCC), the VLSI Circuits Symposium, the European Solid-State Circuits Conference (ESSCIRC), the Radio Frequency Integrated Circuits Symposium (RFIC), and the Asian Solid-State Circuits Conference (A-SSCC). He is/was also a Guest Editor and an Associate Editor of IEEE JOURNAL OF SOLID-STATE CIRCUITS (JSSC), an Associate Editor of IEEE TRANSACTIONS ON MICROWAVE THEORY AND TECHNIQUES (T-MTT), and a Distinguished Lecturer of the IEEE Solid-State Circuits Society (SSCS).

ATSUSHI SHIRANE (Member, IEEE) received the B.E. degree in electrical and electronic engineering and the M.E. and Ph.D. degrees in electronics and applied physics from the Tokyo Institute of Technology, Tokyo, Japan, in 2010, 2012, and 2015, respectively.

From 2015 to 2017, he was with Toshiba Corporation, Kawasaki, Japan, where he developed 802.11ax wireless LAN RF transceiver. From 2017 to 2018, he was with Nidec Corporation, Kawasaki, Japan, where he researched on intelligent motor with wireless communication. He is currently an Associate Professor with the Laboratory for Future Interdisciplinary Research of Science and Technology, Institute of Innovative Research, Tokyo Institute of Technology. His current research interests include RF CMOS transceivers for the IoT, 5G, and satellite communication and wireless power transfer.

Dr. Atsushi is a member of the IEEE Solid-State Circuits Society and the Institute of Electronics, Information and Communication Engineers (IEICE). Since 2019, he has been a member of the technical program committee for IEEE International Solid-State Circuits Conference Student Research Preview.